

# Towards Real-time Adaptive Anisotropic Image-to-mesh Conversion for Vascular Flow Simulations

Kevin Garner\*    Fotis Drakopoulos\*    Chander Sadasivan†    Nikos Chrisochoides\*

## Abstract

Presented is a path towards a fast and robust adaptive anisotropic mesh generation method that is designed to help streamline the discretization of complex vascular geometries within the Computational Fluid Dynamics (CFD) modeling process. The proposed method combines multiple software tools into a single pipeline to provide the following: (1) image-to-mesh conversion which satisfies quality, fidelity, and smoothness requirements, (2) the generation of a boundary layer grid over the high fidelity surface, (3) a parallel adaptive anisotropic meshing procedure which satisfies real-time requirements, and (4) robustness, which is satisfied by the pipeline’s ability to process segmented images and CAD models. The proposed approach is tested with two brain aneurysm cases and is shown to satisfy all the aforementioned requirements. The next steps are to fully parallelize the remaining components of the pipeline to maximize potential performance and to test its integration within a CFD vascular flow simulation. Just as the parallel anisotropic adaptation procedure was tested within aerospace CFD simulations using CAD models, the method is expected to provide accurate results for CFD vascular flow simulations in real-time when executed on multicore cc-NUMA architectures.

## 1 Introduction.

Interventional radiology involves minimally invasive, catheter-based, deployment of several vascular diseases throughout the body. This field has seen an explosion of device technology over the past decade ranging from stent-grafts for aortic aneurysms to valve replacement for diseased cardiac valves. Neuro-interventional radiology, which deals with diseases of the cerebral vasculature, has expanded from the treatment of brain aneurysms to removal of blood clots in large vessel occlusion strokes to embolization of the middle meningeal artery for treatment of chronic subdural hematomas to venous sinus stenting for treatment of idiopathic intracranial hypertension and pulsatile tinnitus. As

hemodynamics are an intrinsic factor of vascular disease, there has been a concomitant increase in the number of studies using Computational Fluid Dynamics (CFD) and/or fluid-structure interactions to better understand disease prognosis or treatment outcomes after deployment of the pertinent medical device. For example, the transport of cardiogenic emboli causing ischemic stroke can be evaluated using imaging scans of the entire vascular branching network in each patient [51]. The recent introduction of miniaturized optical coherence tomography allows for high-resolution imaging of medical device features as well as the vascular wall in any given patient [53], which in turn facilitates high-resolution computational studies of the pathology. CFD may be able to provide clarity in the device treatment of cerebral venous disease, which has irregular morphologies and complex flow patterns [62].

Brain aneurysms (such as that shown in fig. 1) are abnormal focal dilations of intracranial arteries which when left untreated may rupture, resulting in fatal outcomes for patients. Aneurysms have been treated by neuro-interventional devices for nearly three decades, and hence, numerous CFD studies have been conducted on this disease. High resolution CFD simulations provide the opportunity to study hemodynamics in arteries, which can assist clinicians in determining an aneurysm’s potential to rupture and possible methods of treatment (such as the design of neurovascular stents) [52, 13, 17, 12, 36, 46]. Brain aneurysms that form at vascular bifurcations may be subjected to flow instabilities that can only be captured by high-fidelity CFD [41]. Stents used to treat brain aneurysms have wire sizes that can be as small as 25-30 microns with aneurysm sizes ranging from millimeters to centimeters. CFD studies on the effect of such devices (including overlapping devices) on intraneurysmal hemodynamics involve generation of volumetric meshes with elements at multiple sizes [24]. Processing patient-specific medical imaging data of cerebral aneurysms involves the discretization of these complex bodies in the form of smoothed free-form anisotropic body-conforming meshes. Mesh generation methods utilized in commercially available products work well when processing patient-specific

\*Center for Real-time Computing, Old Dominion University, Norfolk, VA 23508, USA

†Cerebrovascular Center for Research, Stony Brook University, Stony Brook, NY 11794, USA

cerebral aneurysm geometries; however, these methods do not always satisfy the time constraints of high resolution CFD simulations.

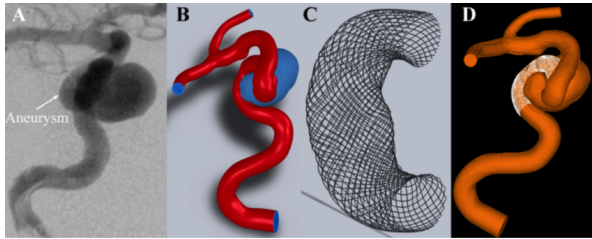


Figure 1: A) an angiogram showing a large  $\sim 25$  mm aneurysm on the right internal carotid artery; B) vasculature segmented in SimVascular [3], lofted in Rhinoceros [2], and imported into SolidWorks [4]; C) flow diverter stent simulated in Matlab with VMTK [9] input; D) vasculature and stent bodies imported into ADINA [1] for mesh generation (also appears in [25]).

These types of medical simulations can be classified into two categories: interactive and predictive. Interactive simulations require real-time mesh generation which can be used to allow surgical residents to practice performing a procedure within a virtual environment. Real-time mesh generation is also required for image registration applications, as they provide guidance to surgeons during operations [21]. Predictive simulations predict and optimize the outcome of an intervention using patient-specific pre-operative image data. Although predictive simulations don't necessarily require real-time mesh generation, both types of simulations are time-sensitive given their impact on a patient's treatment and associated costs.

This paper presents a path towards a fast and robust adaptive anisotropic mesh generation method that is designed to help streamline the discretization of complex vascular geometries and Computer-Aided Design (CAD)-based stents [25, 40] within the CFD modeling process. Several requirements should be addressed with regards to medical image-to-mesh (I2M) conversion: real-time mesh generation, robustness, fidelity, quality, and smoothness. Robustness concerns the software's ability to process different input types such as CAD models (for example, of stents) and patient-specific medical images. Utilizing both is essential when running a CFD vascular flow simulation meant to aid in determining potential methods of treatment [40, 26, 25]. Fidelity measures the degree to which the mesh surface aligns with an image boundary. Quality (determined by the shape and size of mesh elements) and smoothness affect the accuracy of solutions for CFD simula-

tions [10, 32]. Each of these requirements are independently challenging problems. The proposed approach addresses the robustness, fidelity, quality, and (to a degree) smoothness requirements (providing a smoothness of  $C^0$ , as opposed to other available real-time I2M methods that do not address smoothness [31]). Given that the image-to-mesh conversion and boundary layer generation steps are sequential, the proposed approach only addresses the real-time requirement with its parallel adaptive anisotropic mesh generation. After this feasibility study, the next steps will be to fully parallelize all components of the proposed approach in order to maximize potential performance.

The proposed method involves several steps: (1) utilize a method known as CBC3D [27] to discretize a segmented image using a Body-Centered Cubic lattice of high-quality tetrahedra and deform the generated mesh surfaces to their corresponding tissue boundaries to improve fidelity while maintaining quality, (2) construct an anisotropic metric tensor field, (3) generate a boundary layer grid outside the high-fidelity CBC3D mesh surface using a method known as Advancing Front Local Reconnection (AFLR) [48], and (4) utilize a multicore cc-NUMA-based mesh adaptation method known as CDT3D [64] to generate an anisotropic mesh volume using the metric tensor field and CBC3D isotropic mesh as a background mesh. We evaluate this approach using two aneurysm cases (a carotid cavernous aneurysm and middle cerebral artery bifurcation aneurysm) obtained from the Cerebrovascular Center for Research at Stony Brook University under Institutional Review Board approval. We show that the proposed approach meets the aforementioned I2M conversion requirements. Given that CDT3D also exhibited excellent performance and accurately captured features of underlying aerospace simulations when coupled with a solver (processing CAD data such as that shown in fig. 2), the end goal is to utilize this method within a vascular flow simulation.

## 2 Related Work.

There are numerous methods that process medical data as input to create meshes. The type of meshes generated must be taken into account when considering the target application. Meshes can be classified into two categories - structured and unstructured. While some structured mesh generation methods have been shown to provide accurate results within CFD simulations [54, 38, 59], these types of methods can sometimes fail to capture features within complex geometries [11]. Unstructured meshes can be further classified into two categories - isotropic and anisotropic. Isotropic mesh generation methods are well suited for high curvature

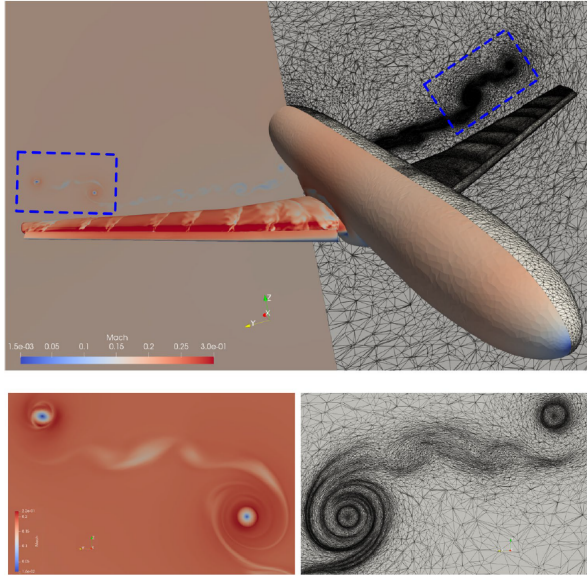


Figure 2: A CDT3D mesh of an aerospace geometry generated from CAD data and its associated solution obtained from a CFD simulation are shown (also appears in [64]).

geometries. Anisotropic meshes contain high aspect ratio elements that include directional information (e.g., hemodynamics). Additionally, they may contain fewer elements in some cases compared to isotropic meshes generated from the same image. A mesh should ideally be as small as possible to reduce the memory and CPU requirements for the solver. These benefits make anisotropic meshes suitable for blood flow problems.

There are many methods that convert 3D images into 3D meshes. For a comprehensive overview of these methods, see [68]. Many 3D isotropic methods utilize Delaunay refinement techniques [14, 56, 34, 60, 16, 58, 18, 31, 63, 30]. A challenge with Delaunay refinement, which still remains an open problem, is that almost flat tetrahedra (slivers) can survive known heuristics designed to remove them [14, 18, 20]. These low quality elements introduce error when processed by a solver. Additional I2M methods utilize lattice space-tree (octree) decomposition techniques [15, 70, 69, 42, 19, 67, 71, 44, 37, 45, 57, 50] to provide meshes with adaptively-sized, high quality elements. Some also utilize the Dual Contouring technique to improve element quality [33, 71, 44, 37, 45]. Others warp the surfaces of the lattice to the boundaries of the object using either a mass-spring system, an FE constitutive model, or an optimization scheme [50, 46, 34]. Some methods focus on processing surface geometries of medical data to create structured Cartesian cut-cell meshes [55] and isotropic

tetrahedral meshes [39]. [29] evaluates several of these sequential isotropic-based methods' suitability for surgical simulations and non-rigid registration applications. There are methods which utilize parallel mesh generation techniques (with either CPUs [45, 54, 38, 59] or GPUs [45]). However, [54, 38, 59] all focus on generating Cartesian cut-cell meshes while [45] focuses on generating isotropic tetrahedral meshes, as with all the aforementioned Delaunay and lattice-based methods. [37] utilizes an anisotropic Giaquinta–Hildebrandt operator-based geometric flow method to smooth mesh surfaces while preserving surface and volume features. However, this smoothing is applied to isotropic meshes.

Some methods focus on converting medical images into anisotropic meshes. Although potentially useful for blood flow simulations, [22] focuses on using an anisotropic mesh adaptation procedure to construct a high-fidelity virtual model of a fractured pelvis, and then to build a physical replica (by means of additive manufacturing techniques) to represent the anatomical object from a segmented image. [16] generates high-quality adaptive hybrid meshes for fluid-solid geometries within cardiac environments. Following segmentation, surfaces between heart tissue and blood (and other non-cardiovascular tissue/fluids) are extracted and adapted. Anisotropic tetrahedra are generated for the interior of heart tissue, a prismatic boundary layer is generated for the interface between tissue and blood, and TetGen (an isotropic boundary-constrained Delaunay-based method [61]) is used to tetrahedralize the remainder of the blood region. Boundary layers in meshes are useful when calculating metrics such as pressure or wall shear stress (WSS) caused by blood flow [52, 16]. Although the method generated high-quality hybrid meshes, the Delaunay-based isotropic elements in fluid flow regions (such as in the coronary arteries) were identified as a drawback, with anisotropy suggested as an improvement. Additionally, Delaunay tetrahedralization limits the quality of the tetrahedral core for complex biological geometries [16] and can fail to terminate for certain cases [27]. Another method was developed to model cerebral aneurysms for fluid-structure interaction simulations [66]. The surface mesh of a healthy blood vessel is deformed onto an aneurysm model, simulating the formation of the aneurysm. While the simulation results demonstrated the benefit of utilizing anisotropic meshes rather than isotropic meshes, the mesh generation method is sequential, as with all the aforementioned adaptive anisotropic methods.

The proposed approach combines multiple software tools into a single pipeline to provide the following: (1) image-to-mesh conversion which satisfies the quality, fidelity, and smoothness ( $C^0$ ) requirements, (2) the

generation of a boundary layer grid over the high fidelity surface, (3) a parallel adaptive anisotropic meshing procedure which satisfies the real-time requirement, and (4) robustness, which is satisfied by the pipeline’s ability to process segmented images and CAD models (such as that shown in fig. 2 [64]). To the best of our knowledge, there is no single method that provides all of the above.

### 3 Background.

**3.1 Image-to-mesh Conversion.** Image-to-mesh conversion is handled by a software called CBC3D [27]. CBC3D converts a segmented, multi-labeled image into an isotropic tetrahedral (or mixed element) mesh. The segmented image is discretized using a regular Body-Centered Cubic lattice. The user has the option of adjusting the distance between the vertices of the lattice. Any resulting tetrahedra located outside the object are discarded. Adaptive refinement commences over these high quality elements using red (regular) - green (irregular) subdivisions. A Euclidean Distance Transform is used to determine if an element should be subdivided. CBC3D allows the user to specify an input fidelity parameter which influences how fine the mesh will be near the boundaries. A label-specific fidelity can also be specified to allow for localized refinement in materials of interest (reducing overall element count). Additionally, a mixed element mesh can be created where tetrahedra are merged into hexahedra. The topology of generated surfaces or interfaces between labels is preserved by only merging within homogenous regions where the lattice is uniform. While useful for further reducing element count, the proposed approach only utilizes tetrahedral meshes generated by CBC3D given that CDT3D (the adaptive anisotropic method) only processes tetrahedral background meshes. As seen in our evaluation (see section 5), CDT3D meets the real-time requirement when processing tetrahedral background meshes. The adaptive refinement approach utilized by CBC3D guarantees an output mesh with high quality elements [27]. CBC3D finally deforms the mesh surfaces to their corresponding image boundaries. The final mesh has a smoothness of  $C^0$  while maintaining the same high quality. Consequently, CBC3D was selected to be the image-to-mesh conversion tool within the pipeline of the proposed approach because it: (1) generates meshes of high quality and fidelity, (2) provides smoothness, and (3) was previously used to discretize patient-specific medical imaging data and STLs of CAD-based stent geometries for use within CFD simulations [40, 26, 25].

**3.2 Boundary Layer Generation.** The generation of boundary layers over the high fidelity CBC3D mesh

surface is carried out by a software known as AFLR. AFLR is an unstructured mesh generation method used extensively in industry. While it is capable of both isotropic [49] and anisotropic mesh generation [47], it is sequential. Consequently, its use within the proposed approach is only focused on its boundary layer generation capability [48]. AFLR generates boundary layers using a spacing that is normal to the boundary and that grows geometrically. As new points are generated, quality is maintained by checking their distribution (i.e., distance from one another according to a local element length scale). New points are only accepted and inserted into the grid if they produce elements that satisfy dihedral angle and element aspect ratio thresholds. The user has numerous options for controlling the spacing distribution and may also specify the number of layers generated.

### 3.3 Adaptive Anisotropic Mesh Generation.

The final adaptive anisotropic mesh is generated using a software tool called CDT3D. CDT3D is a multicore cc-NUMA-based mesh generation method that exploits fine-grain parallelism at the cavity level using data decomposition. It is capable of both isotropic [28] and adaptive anisotropic mesh generation [64]. A speculative execution model is implemented, which serves to exploit parallelism “everywhere possible” throughout the mesh generation procedure. Atomic lock instructions are utilized by several of CDT3D’s meshing operations so that different data can be modified concurrently while guaranteeing correctness (i.e., conformity). A lock attempts to acquire the necessary dependencies for a corresponding operation. If unable to do so, any acquired resources are released and the operation is applied on a different set of data. This is repeated until the mesh satisfies spacing and qualitative criteria. There are a number of parallel mesh operations in CDT3D, including: edge collapse, point creation/insertion (which by default uses an advancing front technique for isotropic mesh generation and a centroid-based technique for anisotropic adaptation), CAD projection, local reconnection (edge/face swapping), and point smoothing. See [28] and [64] for more information on their design and implementation.

CDT3D accepts an analytic or discrete metric field as input when performing metric-based anisotropic mesh adaptation. CAD geometries can also be processed and used to perform adaptation (thus allowing the proposed approach to handle both medical I2M conversion and the processing of CAD models for CFD simulations involving stents). CDT3D has been quantitatively and qualitatively evaluated with several benchmarks based on aerospace cases [65, 64]. Not only was



it shown to be stable in terms of metric conformity (element shape size and edge length), it also showcased excellent performance when utilizing up to 40 cores on a single multicore node. When coupled with a solver in a CFD simulation pipeline, it captured features of the underlying simulation and occupied only a small fraction of the pipeline’s runtime [64] (a visual example is shown in fig. 2).

#### 4 Method.

The proposed approach involves several steps: (1) utilize CBC3D to convert a segmented image into a high quality and high fidelity background mesh (for anisotropic mesh adaptation), (2) construct an anisotropic metric tensor field, (3) generate a boundary layer grid outside the CBC3D mesh surface using AFLR, and (4) utilize CDT3D to generate an anisotropic mesh volume using the metric tensor field. A visual overview of this pipeline of tools can be seen in fig. 3.

The proposed approach is not bound to any particular method for constructing the metric tensor field. As stated previously, the pipeline is evaluated based on the aforementioned requirements to gauge its suitability for CFD vascular flow simulations. Consequently, our method is tested using two different techniques for constructing a metric tensor field, where each is used with a different aneurysm case. These techniques are described in our experimental setup, section 5.1. The anisotropic metric tensor field and CBC3D background volume mesh (converted from the segmented image) are provided as input to CDT3D, which generates an adaptive anisotropic volume mesh. In this study, surface adaptation is turned off to ensure that the high fidelity surface generated by CBC3D remains intact. The surface is extracted from the CBC3D mesh and is given as input to AFLR to generate a boundary layer grid. AFLR is set to only generate a boundary layer grid, designating the input as an open domain so that only boundary layer elements are generated on the outside of the surface. Surface refinement is also turned off for AFLR (again, for this particular study) to ensure that the high fidelity CBC3D surface remains intact and so that both the boundary layer grid and CDT3D mesh are conforming. The two are merged to create one final output mesh.

#### 5 Results.

**5.1 Experimental Setup.** The first aneurysm case is based on a rotational angiography scan of a carotid cavernous aneurysm with image spacing of  $1.00 \times 1.00 \times 1.00 \text{ mm}^3$  and an image size of  $512 \times 512 \times 508$  voxels<sup>3</sup>. The CBC3D mesh generated from it can be seen in fig. 6(a), in addition to its approximate

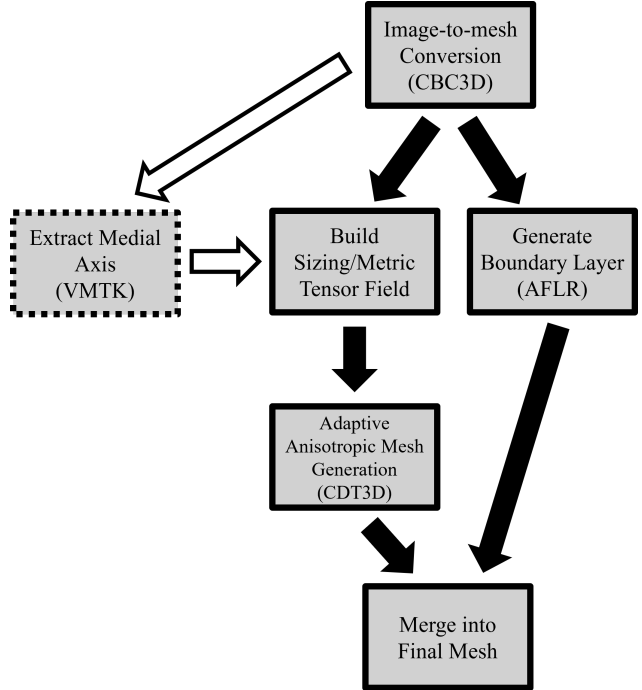


Figure 3: Presented is the pipeline of software tools used to satisfy the medical image-to-mesh conversion requirements for use within a CFD vascular flow simulation. It begins with image-to-mesh conversion (handled by CBC3D). Extracting the medial axis with VMTK [9, 8] is optional, as the method in [21] is only used to build an anisotropic metric tensor field for the purpose of testing this pipeline’s capability to meet the aforementioned requirements (described in section 5.1). A boundary layer grid is generated over the CBC3D mesh using AFLR while the adaptive anisotropic mesh volume is generated by CDT3D (using the CBC3D mesh as a background mesh). The boundary layer grid and anisotropic mesh are merged into one final mesh.

medial axis. The second case is a surface mesh of a middle cerebral artery bifurcation aneurysm given as a Piecewise Linear Complex (PLC) in a .stl format (seen in fig. 4(d)). The full pipeline of the proposed approach is tested with the first case while each method attempts to perform mesh generation/adaptation using only the surface mesh for the second case. All codes were compiled using GNU GCC 7.5.0. Data were collected on Old Dominion University’s Wahab cluster using a dual socket node that features two Intel<sup>®</sup> Xeon<sup>®</sup> Gold 6148 CPUs @ 2.40 GHz (20 slots) and 384GB of memory. For a performance evaluation, each run in the following experiments was executed five times and the results were averaged.

We evaluate the adaptive anisotropic mesh generation method with metric tensor fields that are constructed using different techniques. For the first case, an anisotropic metric tensor field is constructed based on a method also utilized for non-rigid registration applications intended for image-guided neurosurgery [21]. This method focuses on capturing registration points within an adaptive mesh. A metric tensor field is built by evaluating the  $k$ -closest registration points to each mesh vertex using a  $k$ -nn search from the VTK library [6]. The Khachiyan algorithm is then used to construct a minimum volume bounding ellipsoid which encompasses the given point set. This ellipsoid has a natural mapping to a  $3 \times 3$  positive definite matrix that can be used as a metric to guide adaptivity. See [21] for more details. To exploit parallelism, an OpenMP construct is utilized when processing the mesh points. For our first test case, we utilize this method using the points of an approximate medial axis of the generated CBC3D mesh (in place of registration points). The approximate medial axis (also called a centerline) is obtained for our first test case using VMTK [9, 8] and can be seen in fig. 6(a).

Figure 4 shows the vascular structure imaged by rotational angiography of the right carotid artery for the second aneurysm case, in addition to the surface mesh (utilized in this study) obtained from a segmentation of the region of interest. Figure 5 shows streamline data from a CFD simulation for this case (executed outside of this study [43]). The velocity at each point along these streamlines is used to construct a metric tensor field to guide adaptivity for anisotropic mesh generation. A velocity gradient tensor is calculated at each point which can be mapped to a  $3 \times 3$  positive definite matrix. The magnitude (eigenvalue) of each velocity gradient tensor is used to apply a stretching factor to the positive definite matrix which ensures that elements are stretched in the dominant direction of the velocity. An isotropic volume mesh is first generated using the surface mesh of the second case. A  $k$ -nn search is utilized to find the 3 closest velocity points to each mesh volume vertex (which are then used to calculate the velocity gradient tensor for each mesh point). OpenMP is again utilized to parallelize the processing of the mesh points. The isotropic volume mesh is processed as a background mesh with the velocity-based metric tensor field to generate anisotropic meshes. Both the anisotropic and isotropic meshes generated by CDT3D for the second case are evaluated.

**5.2 Quantitative and Qualitative Analysis** The results obtained from CDT3D are also compared to TetGen [61, 5] (replacing the adaptive anisotropic method

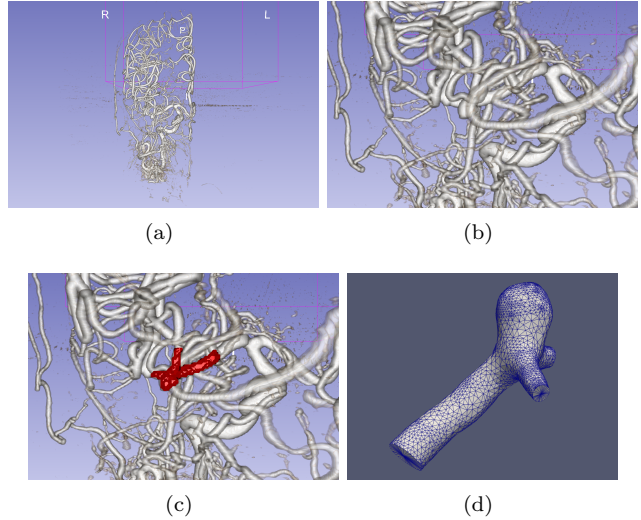


Figure 4: The original image of the second aneurysm case is shown from an anteroposterior view. (a) shows the vascular structure imaged by rotational angiography of the right carotid artery. (b) zooms in to the region of interest while (c) highlights the PLC obtained from the segmentation of the aneurysm. (d) shows only the resulting PLC.

with this adaptive isotropic method in the pipeline). TetGen is a sequential, Delaunay-based method that generates isotropic tetrahedral meshes. In addition to an anisotropic metric field, an isotropic sizing function is also constructed (based on the aforementioned approach in [21]) specifically for TetGen. We compare results between meshes generated by TetGen when it utilizes this sizing function and when it does not (tetrahedralization of the CBC3D surface). Additionally, we compare the TetGen isotropic meshes to isotropic meshes generated by CDT3D (again simply processing the same surface as a PLC - .stl).

Table 1 shows the parameters used for each mesh generation method in the pipeline (except CBC3D). The first aneurysm case was also used to evaluate CBC3D in [27] (as it was compared to other isotropic I2M conversion methods from industry and academia). The same parameters utilized for CBC3D in that study are utilized in this evaluation. A wide range of values were tested for the value of  $k$  used in the  $k$ -nn search when building the sizing function and metric tensor fields for the first case. The optimal parameters were determined based on the best quality mesh that was generated. If certain parameters are not listed in table 1, then their default value was utilized. The optimal value for  $k$  with the isotropic runs of TetGen is 30. The optimal value for  $k$  in the metric-adapted anisotropic runs of CDT3D

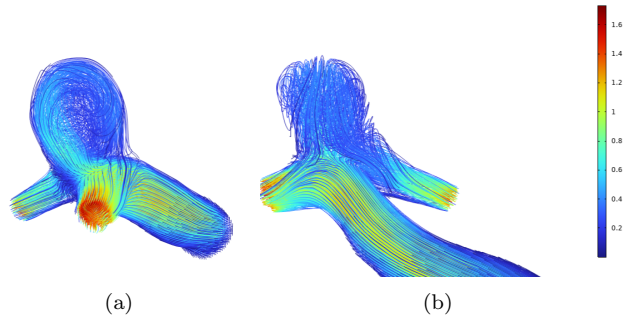


Figure 5: Shown is streamline data of the velocity field from a CFD simulation with the second aneurysm case. (a) and (b) show different viewpoints. The velocity color legend is in m/s [43].

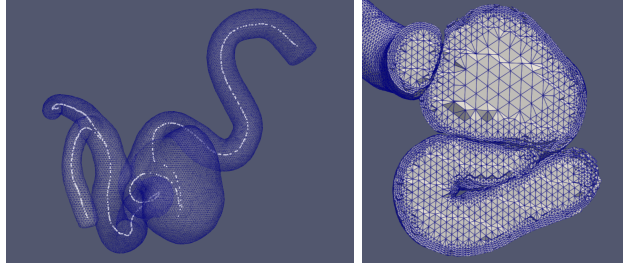
is 40. The CDT3D parameters  $nqual$  and  $nsmth$  were both increased to 10 while  $cdfn$  was changed to 0.8 to improve the final anisotropic mesh quality for the second aneurysm case (with no surface adaptation by CDT3D, explained later).

CBC3D takes approximately 61.59 seconds (1 min) to convert the segmented image of the first aneurysm into a mesh of approximately 272K tetrahedra and 63K points. Figure 6 shows cross sections of the volume meshes generated by each method, merged with the conforming AFLR boundary layer mesh. Figure 7 shows cross sections of the volume meshes generated for the second aneurysm case. Table 2 shows the number of elements generated by each method when processing the CBC3D mesh of aneurysm 1 and the surface mesh of aneurysm 2. The TetGen meshes contain fewer elements compared to the CDT3D meshes in both cases. Table 3 and table 4 show the runtime of each method for aneurysm cases 1 and 2, respectively. They also show the mesh generation/adaptation rates of each method (measured in elements generated per second). TetGen exhibits good performance when generating its small-size meshes. Although it is not listed in table 3, it should be noted that CDT3D exhibits good scalability, as its runtime is reduced to approximately 1 minute and its anisotropic adaptation rate becomes 27K when utilizing 40 cores. When utilizing 10 cores, CDT3D’s mesh generation/adaptation rate exceeds that of TetGen’s. For the second case, CDT3D completes anisotropic adaptation in about 49 seconds when utilizing 40 cores.

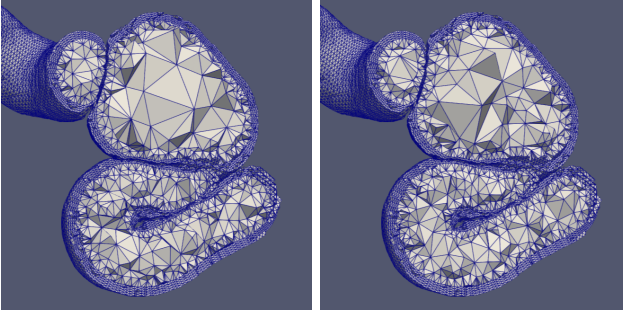
Mesh fidelity is evaluated using a two-sided Hausdorff Distance (HD) metric (based on an open source implementation [23]):  $HD = \max\{HD_{I \rightarrow M}, HD_{M \rightarrow I}\}$ , where  $HD_{I \rightarrow M}$  is the value of the metric from the image to the mesh, and  $HD_{M \rightarrow I}$  is the value of the metric

Table 1: Input parameters for each mesh generation method utilized in the pipeline (after CBC3D). Val. is an abbreviation for value.

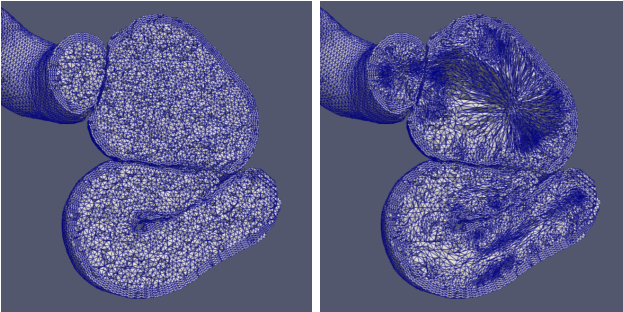
Method	Parameter/Val.	Description
TetGen (iso-sizing)	r	reconstruct mesh
	m	use sizing
	q	optimize quality
	R	reduce elements
	O/9	optimize mesh
TetGen (iso)	Y	freeze surface
	P	mesh plc
	q	improve quality
	R	reduce elements
	O/9	optimize mesh
AFLR (bl)	Y	freeze surface
	mbl/1	boundary layer
	blds/1.2	initial bl spacing
	(for case 1)	
	blds/0.12	initial bl spacing
CDT3D (iso)	(for case 2)	
	fints/0,	freeze surface
	open	only bl
	sref/0	freeze surface
	nthreads/*	parallel threads
CDT3D (aniso)	met/1	use metric
	meval/1	metric-vertices
	sref/0	freeze surface
	reconstruct/1	reconstruct mesh
	mpp/5	point creation
		method - centroid
	cdff/1.2	edge length mult.
	cdfn/0.6	nearby node dist.
	nqual/3	optimize quality
	nsmth/5	smooth points
nthreads/*	parallel threads	



(a) CBC3D mesh with an approximate medial axis (b) CBC3D Volume mesh

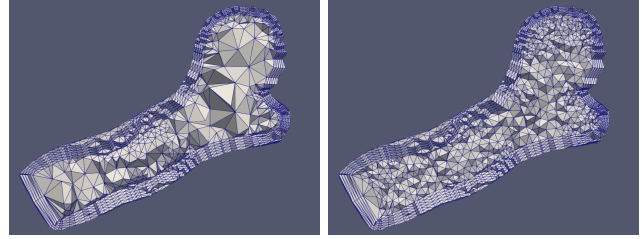


(c) TetGen (isotropic from PLC) (d) TetGen (isotropic with sizing function)

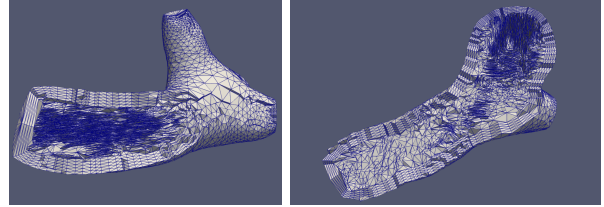


(e) CDT3D (isotropic from PLC) (f) CDT3D (anisotropic with metric tensor field)

Figure 6: Cross sections are shown of the volume meshes generated by each method for the first aneurysm case, merged with the conforming boundary layer mesh generated by AFLR.



(a) TetGen (isotropic from PLC) (b) CDT3D (isotropic from PLC)



(c) CDT3D (anisotropic with velocity-based metric tensor field) view 1 (d) CDT3D (anisotropic with velocity-based metric tensor field) view 2

Figure 7: Cross sections are shown of the volume meshes generated by each method for the second aneurysm case, merged with the conforming boundary layer mesh generated by AFLR.

from the mesh to the image. A low HD error indicates a high fidelity. Hausdorff Distance is computed between two point sets. The first point set contains the vertices located on the mesh surface and the second point set contains the voxels located on the boundaries of the segmented material. For the first aneurysm case (in fig. 6(a)),  $HD_{I \rightarrow M}$  is 4.51 while  $HD_{M \rightarrow I}$  is 1.74. The HD is therefore 4.51. The fidelity of the mesh generated by CBC3D was also evaluated for the first aneurysm case in [27]. CBC3D was compared to several highly used I2M methods, exhibiting good fidelity while maintaining better smoothness compared to the other methods' meshes. Surface refinement/adaptation is turned off for all mesh generation methods tested in this pipeline (except CBC3D). This ensures that the high fidelity and smooth surface generated by CBC3D remains intact.

For the isotropic meshes, qualitative results are examined with respect to element dihedral angles. Figure 8 compares the quality of the isotropic meshes generated by each method for case 1 and fig. 9 compares those generated for case 2. Table 5 shows the smallest and largest dihedral angles found in the isotropic meshes generated by each method. The CDT3D meshes contain better quality compared to the TetGen meshes. This is particularly seen in (b) and (c) of fig. 8 and fig. 9, which show that the TetGen meshes contain more elements

Table 2: Number of tetrahedra and points generated by each method when processing the CBC3D mesh converted from the segmented image of the first aneurysm and the surface mesh of the second aneurysm. ‘Tets’ is short for tetrahedra. K means thousand and M means million.

Methods		Aneurysm 1	Aneurysm 2
TetGen (iso-sizing)	Tets	120K	-
	Points	37K	-
TetGen (iso)	Tets	118K	12K
	Points	36K	3K
AFLR (bl)	Tets	805K	105K
	Points	144K	18K
CDT3D (iso)	Tets	631K	31K
	Points	122K	7K
CDT3D (aniso)	Tets	1.59M	80K
	Points	284K	15K

Table 3: The time spent (approximately in **minutes**) and the number of elements generated per second by each method (in parentheses) for small-size meshes is shown when processing the CBC3D mesh converted from the segmented image of the first aneurysm. Instead of elements per second, the values in parentheses for Build\_Sizing/Metric represent the CBC3D volume mesh points processed per second. K means thousand.

Methods	CPU Cores		
	1	10	20
Build_Sizing/Metric	191 (5K)	19 (55K)	9 (117K)
TetGen (iso-sizing)	0.1 (20K)	-	-
TetGen (iso)	0.06 (32K)	-	-
AFLR (bl)	0.2 (67K)	-	-
CDT3D (iso)	0.6 (17K)	0.3 (42K)	0.1 (78K)
CDT3D (aniso)	20 (1K)	3 (8K)	2 (14K)

with small and large angles. For the adapted anisotropic meshes, qualitative results are examined with respect to their metric conformity. The goal of metric conformity is to create a unit grid, where edges are unit-length and elements are unit-volume with respect to the target metric. For calculating edge length, we adopted the same definition that appears in [7]. For two vertices  $a$  and  $b$ , an edge length in the metric  $L_e$  can be evaluated using:

$$(5.1) \quad L_e = \begin{cases} \frac{L_a - L_b}{\log(L_a/L_b)} & |L_a - L_b| > 0.001 \\ \frac{L_a + L_b}{2} & \text{otherwise} \end{cases}$$

$$L_a = (v_e^T M_a v_e)^{\frac{1}{2}}, L_b = (v_e^T M_b v_e)^{\frac{1}{2}}$$

and an element mean ratio shape measure can be approximated in the discrete metric as:

Table 4: The time spent (approximately in **seconds**) and the number of elements generated per second by each method (in parentheses) for small-size meshes is shown when processing the surface mesh of the second aneurysm. K means thousand.

Methods	CPU Cores		
	1	10	20
TetGen (iso)	1.54 (8K)	-	-
AFLR (bl)	1.8 (58K)	-	-
CDT3D (iso)	2.2 (14K)	1.73 (18K)	1.24 (25K)
CDT3D (aniso)	910 (87)	105 (761)	69 (1K)

$$(5.2) \quad Q_k = \frac{36}{3^{1/3}} \frac{\left(|k| \sqrt{\det(M_{mean})}\right)^{\frac{2}{3}}}{\sum_{e \in L} v_e^T M_{mean} v_e},$$

where  $v$  is a vertex of element  $k$  and  $M_{mean}$  is the interpolated metric tensor evaluated at the centroid of element  $k$ . Given that optimal edges should be unit-length, edges with length above or below one are considered to be sub-optimal. The measure for mean ratio is bounded between zero and one since it is normalized by the volume of an equilateral element. One is the optimal quality for an element’s mean ratio shape. Figure 10 shows that CDT3D maintains good quality when generating an anisotropic mesh for the first case. Although there are 3 elements with a mean ratio measure less than 0.1 (the minimum shape measure is 0.016), the majority of elements have a high mean ratio and edge lengths close to 1. With regards to the second case, the anisotropic mesh generated by CDT3D exhibits poor quality when the surface of the input mesh is not adapted (containing about 1K elements with a mean ratio less than 0.1). However, when CDT3D is permitted to adapt the surface, the final mesh quality is much better (about 20 elements have a mean ratio less than 0.1, with the minimum shape measure as 0.042). When adapting the surface, the same parameters as those in table 1 are utilized with surface adaptation turned on. It should be noted that CDT3D converges and completes anisotropic adaptation in less time when surface adaptation is permitted (generating 90K tetrahedra in about 22 seconds when utilizing 20 cores) as opposed to its performance when restricting the method to preserve the input surface. The quality of the CDT3D mesh generated for the first case shows that CBC3D indeed generates a mesh of good quality when converting the first case image, given that surface adaptation is turned off for CDT3D and it still generates a final volume of good quality. In order to provide a volume that conforms to the boundary layer grid generated by AFLR, surface adaptation is turned off



and CDT3D is therefore limited by the quality of the input surface mesh for the second aneurysm case. It should be noted that surface adaptation was attempted first, where the CDT3D-adapted surface was provided as input to AFLR. However, AFLR failed to process the CDT3D-adapted surface and generate a boundary layer grid. We also attempted surface refinement and volume generation using AFLR, to then subsequently use as a background mesh for CDT3D’s anisotropic adaptation (which could potentially be merged with a boundary layer grid generated over the AFLR-refined surface). AFLR however fails to refine the input PLC surface of the second case. Nevertheless, the majority of elements in both anisotropic meshes generated by CDT3D for the second aneurysm case (with and without surface adaptation) have a high mean ratio and edge lengths close to 1.

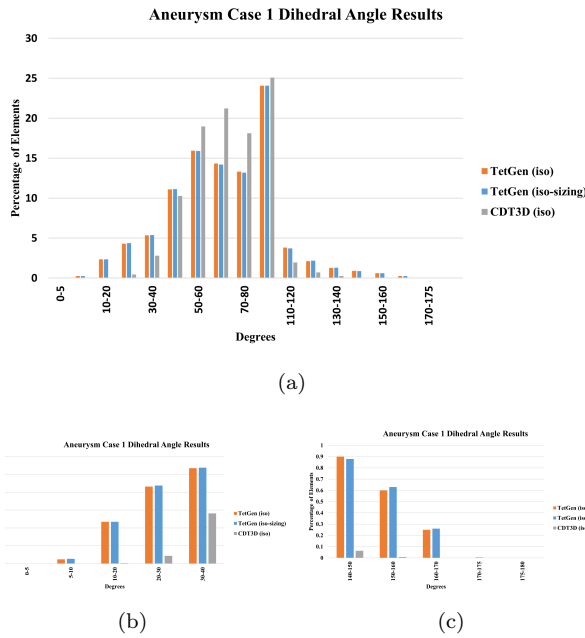


Figure 8: Quality statistics are shown comparing the dihedral angles of the isotropic meshes generated by TetGen and CDT3D for the first aneurysm case. (a) shows the full distribution of element dihedral angles. (b) shows the distribution of elements with dihedral angles between 0 and 40 degrees. (c) shows the distribution of elements with dihedral angles between 140 and 180 degrees.

## 6 Discussion and Future Work.

Although it doesn’t generate anisotropic meshes, TetGen exhibits good quality while generating much fewer elements compared to CDT3D (for the small test cases

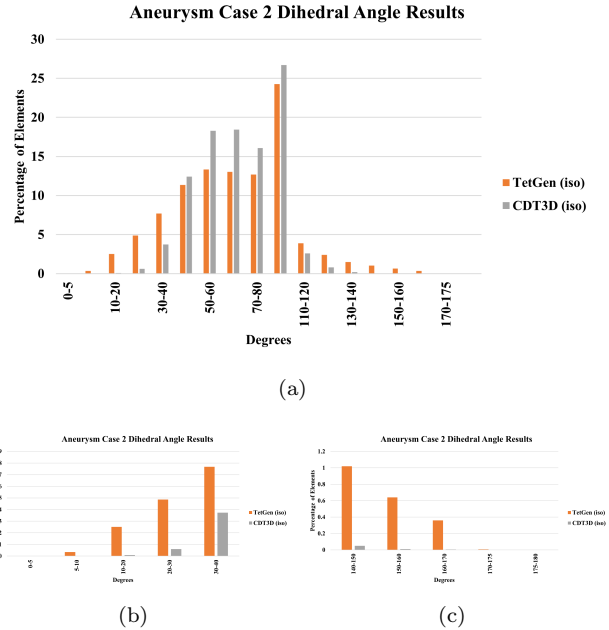


Figure 9: Quality statistics are shown comparing the dihedral angles of the isotropic meshes generated by TetGen and CDT3D for the second aneurysm case. (a) shows the full distribution of element dihedral angles. (b) shows the distribution of elements with dihedral angles between 0 and 40 degrees. (c) shows the distribution of elements with dihedral angles between 140 and 180 degrees.

of our evaluation). Additionally, TetGen meets the real-time requirement for small-size problems. CDT3D generates meshes with better quality but at the cost of generating more elements. Depending on the accuracy needed for CFD simulations, this tradeoff may be acceptable, particularly when combined with CDT3D’s anisotropy (seen in fig. 6 and fig. 7). Both the Build.Sizing/Metric and CDT3D methods show good scalability on a single multicore node, particularly when generating an anisotropic mesh. Due to the fact that CDT3D is designed to handle much larger problems (such as that in fig. 2 and fig. 4), its performance suffers from the overhead of parallelizing adaptation for such small meshes. Nevertheless, it also meets the real-time requirement when utilizing a full multicore node (for anisotropic mesh adaptation) and when utilizing a single CPU core for isotropic mesh generation. CDT3D exhibits much faster performance when generating isotropic meshes from the PLCs of the first and second cases.

The parallelism offered by CDT3D would be well suited for processing a geometry generated from an im-

Table 5: Smallest and largest dihedral angles in isotropic meshes generated by TetGen and CDT3D for both aneurysm cases.

Methods	Angle	Aneurysm 1	Aneurysm 2
TetGen (iso-sizing)	Smallest	1.67	-
	Largest	176.73	-
TetGen (iso)	Smallest	3.99	2.71
	Largest	171.66	171.3
CDT3D (iso)	Smallest	3.99	3.54
	Largest	165.25	172.93

age of a large vascular structure (such as in fig. 4). This would likely require many more elements compared to the small test cases of this study. Consequently, additional memory would also be required, potentially necessitating the need for a distributed memory approach (such as [35]) if a sequential or multicore cc-NUMA-based method cannot generate and store such a large mesh within the memory of a single machine (millions of elements, or potentially hundreds of millions of elements which in the future may be needed for aneurysm cases requiring even finer mesh resolution, e.g., microvascular aneurysms). Table 3 shows the elements generated per second up to 20 cores by CDT3D for the first aneurysm case. As mentioned previously, the adaptation rate becomes 27K when utilizing 40 cores. For comparison, TetGen generates 20K isotropic elements per second (when using the sizing function for adaptivity). Consider an example where a vascular structure requires a mesh of 10 million elements in order to obtain the needed accuracy in a CFD simulation. Based on the above rates, TetGen would take approximately 8 minutes (or 83 minutes in the case of a 100 million element mesh) to generate an adaptive isotropic mesh while CDT3D would take approximately 6 minutes (or 61 minutes for 100 million elements) to generate an adaptive anisotropic mesh using 40 cores. Furthermore, CDT3D utilizes a similar speculative execution model (described in section 3.3) that was utilized within the I2M method in [31]. With an additional hierarchical work-stealing optimization for load balancing, this model for parallelization was tested and shown to maintain a speedup of approximately 123 when executed on a distributed shared memory architecture using 144 cores (seen in table 4 of [31]). If CDT3D were to receive a similar optimization and be executed on a similar architecture, it could potentially achieve an adaptation rate of 98K elements per second (based on the rates seen thus far in table 3), generating approximately 10 million anisotropic elements in 1.7 minutes (100 million elements in 17 minutes). CDT3D’s adaptation rate, coupled with its scalable performance and better qual-

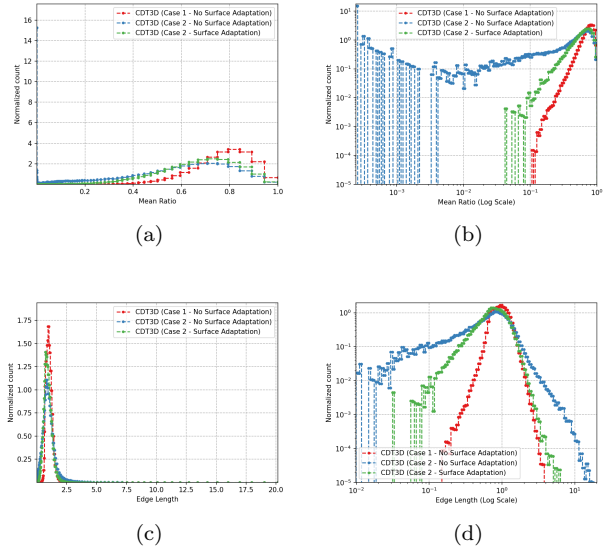


Figure 10: Shown are distributions of quality statistics for the mean ratio, (a) and (b), and edge lengths, (c) and (d), of elements within the anisotropic meshes generated by CDT3D for both aneurysm cases (in linear and logarithmic scales). A good quality mesh is indicated if most of its elements have a mean ratio shape measure and edge length size close to 1.

ity, may prove beneficial when anisotropy is needed to provide better simulation results compared to isotropy (such as in [66, 16]). Future work is required to optimize and test CDT3D on a distributed shared memory architecture in order to gauge its potential and verify this performance estimation.

Although the methods utilized in the proposed approach have been shown to satisfy the I2M requirements using the small test cases in our evaluation, additional experimentation (and fine-tuning of each method’s parameters) is required to process larger test cases (such as the complete vascular structure in fig. 4(a)). The mesh deformation scheme employed by our I2M approach produces meshes with a smoothness of  $C^0$ . This smoothness is sufficient for aneurysm geometries such as those in our evaluation [27]; however, future work is required to improve the smoothness of geometries reconstructed from micro-CT images (i.e., some stent geometries). Our approach must be updated to provide a smoothness of  $C^1$ . Given CDT3D’s ability to process CAD models (such as in fig. 2), this approach remains to be tested within a CFD vascular flow simulation that includes CAD models of stents (testing potential avenues of treatment for other aneurysm cases).

Eventually, the tools utilized in the pipeline of the

proposed approach should be integrated into a single software. It should be noted that conversions are required between the input and output files of the methods utilized. For example, several of the methods use the VTK library [6]. Because they were each developed at different time periods, one method produces output utilizing a newer version of the library while another (which utilizes an older version) needs to read this as input. Although the conversion times for the small test cases in our evaluation are negligible, this discrepancy between the methods will likely negatively impact performance when the pipeline is tested on large cases. Integrating these methods into a single software will not only eliminate this problem, but will remove the complexity of compiling all codes separately and running them one after the other in the pipeline. Rather than separating image-to-mesh surface adaptation from anisotropic volume generation (and freezing the surface during this step), it would be more effective to perform both simultaneously when converting the segmented image (similar to the isotropic approach in [31]). If integrated with a boundary layer generation method, this can help prevent the inhibition of mesh quality improvement (such as that shown for the second aneurysm case in fig. 10). Finally, the sequential methods must be parallelized (or replaced with other parallel methods) in order to maximize potential performance, especially for large cases.

## 7 Conclusion.

Presented is a path towards a fast and robust adaptive anisotropic mesh generation method that is designed to help streamline the discretization of complex vascular geometries and CAD-based stent models within the CFD modeling process. The proposed approach combines multiple software tools into a single pipeline to provide the following: (1) image-to-mesh conversion which satisfies quality, fidelity, and smoothness requirements, (2) the generation of a boundary layer grid over the high fidelity surface, (3) a parallel adaptive anisotropic meshing procedure which satisfies the real-time requirement, and (4) robustness, which is satisfied by the pipeline's ability to process segmented images and CAD models. This pipeline is tested on a segmented image of a carotid cavernous aneurysm. Additionally, the parallel meshing method is also tested using a surface mesh of a middle cerebral artery bifurcation aneurysm. Both aneurysm cases were obtained from the Cerebrovascular Center for Research at Stony Brook University under Institutional Review Board approval. The pipeline is shown to satisfy all the aforementioned requirements. More specifically, the parallel mesh generation method successfully produces

high quality isotropic and anisotropic meshes for the aneurysm cases in real-time. Having shown the feasibility of this approach with regards to these requirements, the next steps are to fully parallelize the remaining components of the pipeline to maximize potential performance and to test its integration within a CFD vascular flow simulation. Just as the parallel anisotropic adaptation procedure was tested within aerospace CFD simulations using CAD models (such as that shown in fig. 2 [64]), the method is expected to provide accurate results for CFD vascular flow simulations in real-time when executed on multicore cc-NUMA architectures.

## Acknowledgements

This research was sponsored by the Richard T. Cheng Endowment at Old Dominion University, SURA grant No. C2024-FEMT-011-01, and the National Institute of General Medical Sciences of the National Institutes of Health under Award Number 1T32GM140911-03. This study was also partially supported by a pilot award from the Long Island Network for Clinical and Translational Science. The content is solely the authors' responsibility and does not necessarily represent the official views of the National Institutes of Health. Additionally, this work was supported by the research computing clusters at Old Dominion University. The authors would like to thank Dr. Christos Tsolakis for helping to assemble the tools utilized in the adaptive pipeline of our approach. We'd also like to thank Dr. David Marcum for sharing the AFLR software utilized in this study, and Evangelia Frastali for helping to determine the best parameters for each method tested in our evaluation.

## References

- [1] *Adina: Finite element analysis software*. <https://www.bentley.com/software/adina/>, 2024. Accessed: 10/12/2024.
- [2] *Rhino - rhinoceros 3d*. <https://www.rhino3d.com/>, 2024. Accessed: 10/12/2024.
- [3] *Simvascular*. <https://simvascular.github.io/>, 2024. Accessed: 10/12/2024.
- [4] *Solidworks: 3d cad design software and pdm systems*. <https://www.solidworks.com/>, 2024. Accessed: 10/12/2024.
- [5] *Tetgen: A quality tetrahedral mesh generator and a 3d delaunay triangulator*. <https://wias-berlin.de/software/index.jsp?id=TetGen&lang=1>, 2024. Accessed: 10/9/2024.
- [6] *Vtk*. <https://www.vtk.org/>, 2024. Accessed: 10/1/2024.
- [7] F. ALAUZET, *Size gradation control of anisotropic meshes*, Finite Elements in Analysis and Design, 46 (2010), pp. 181–202. Mesh Generation - Applications and Adaptation.

- [8] L. ANTIGA, B. ENE-LORDACHE, AND A. REMUZZI, *Centerline computation and geometric analysis of branching tubular surfaces with application to blood vessel modeling*, in 11-th International Conference in Central Europe on Computer Graphics and Visualization, Plzen, Czech Republic, 2003.
- [9] L. ANTIGA, M. PICCINELLI, L. BOTTI, B. ENE-IORDACHE, A. REMUZZI, AND D. STEINMAN, *An image-based modeling framework for patient-specific computational hemodynamics*, *Medical & Biological Engineering & Computing*, 46 (2008), pp. 1097–1112.
- [10] I. BABUŠKA AND A. K. AZIZ, *On the angle condition in the finite element method*, *SIAM Journal on Numerical Analysis*, 13 (1976), pp. 214–226.
- [11] S. B. BADEN, N. P. CHRISOCHOIDES, D. B. GANNON, AND M. L. NORMAN, *Structured Adaptive Mesh Refinement (SAMR) Grid Methods*, Springer, New York, NY, 1999.
- [12] Y. BAZILEVS, M.-C. HSU, Y. ZHANG, W. WANG, T. KVAMSDAL, S. HENTSCHEL, AND J. ISAKSEN, *Computational vascular fluid–structure interaction: methodology and application to cerebral aneurysms*, *Biomechanics and Modeling in Mechanobiology*, 9 (2010), pp. 481–498.
- [13] P. BERG, S. SAALFELD, S. VOSS, O. BEUING, AND G. JANIGA, *A review on the reliability of hemodynamic modeling in intracranial aneurysms: why computational fluid dynamics alone cannot solve the equation*, *Neurosurgical Focus*, 47 (2019).
- [14] D. BOLTICHEVA, M. YVINEC, AND J.-D. BOISSONNAT, *Mesh generation from 3D multi-material images*, in *Medical Image Computing and Computer-Assisted Intervention – MICCAI 2009*, G.-Z. Yang, D. Hawkes, D. Rueckert, A. Noble, and C. Taylor, eds., vol. 5762 of *Lecture Notes in Computer Science*, Springer Berlin Heidelberg, London, UK, 2009, pp. 283–290.
- [15] J. BRONSON, J. LEVINE, AND R. WHITAKER, *Lattice cleaving: A multimaterial tetrahedral meshing algorithm with guarantees*, *IEEE Transactions on Visualization and Computer Graphics*, 20 (2014), pp. 223–237.
- [16] J. P. CARSON, A. P. KUPRAT, X. JIAO, V. DYE-DOV, F. D. PIN, J. M. GUCCIONE, M. B. RATCLIFFE, AND D. R. EINSTEIN, *Adaptive generation of multimaterial grids from imaging data for biomedical lagrangian fluid–structure simulations*, *Biomechanics and Modeling in Mechanobiology*, 9 (2010), pp. 187–201.
- [17] J. CEBRAL AND R. LOHNER, *Efficient simulation of blood flow past complex endovascular devices using an adaptive embedding technique*, *IEEE Transactions on Medical Imaging*, 24 (2005), pp. 468–476.
- [18] S.-W. CHENG, T. K. DEY, H. EDELSBRUNNER, M. A. FACELLO, AND S.-H. TENG, *Silver exudation*, *Journal of the ACM (JACM)*, 47 (2000), pp. 883–904.
- [19] A. N. CHERNIKOV AND N. P. CHRISOCHOIDES, *Multitissue tetrahedral image-to-mesh conversion with guaranteed quality and fidelity*, *SIAM Journal on Scientific Computing*, 33 (2011), pp. 3491–3508.
- [20] L. P. CHEW, *Guaranteed-quality Delaunay meshing in 3D (short version)*, in *Proceedings of the Thirteenth Annual Symposium on Computational Geometry*, SCG ’97, New York, NY, USA, 1997, ACM, pp. 391–393.
- [21] N. CHRISOCHOIDES, Y. LIU, F. DRAKOPOULOS, A. KOT, P. FOTEINOS, C. TSOLAKIS, E. BILLIAS, O. CLATZ, N. AYACHE, A. FEDOROV, A. GOLBY, P. BLACK, AND R. KIKINIS, *Comparison of physics-based deformable registration methods for image-guided neurosurgery*, *Frontiers in Digital Health*, 5 (2023), pp. 481–498.
- [22] F. CLERICI, N. FERRO, S. MARCONI, S. MICHELETTI, E. NEGRELLO, AND S. PEROTTO, *Anisotropic adapted meshes for image segmentation: Application to three-dimensional medical data*, *SIAM Journal on Imaging Sciences*, 13 (2020), pp. 2189–2212.
- [23] F. COMMANDEUR, J. VELUT, AND O. ACOSTA, *A VTK algorithm for the computation of the Hausdorff distance*, *The VTK Journal*, (2011).
- [24] R. DAMIANO, V. TUTINO, N. PALIWAL, D. MA, J. DAVIES, A. SIDDIQUI, AND H. MENG, *Compacting a single flow diverter versus overlapping flow diverters for intracranial aneurysms: A computational study*, *American Journal of Neuroradiology*, 38 (2017), pp. 603–610.
- [25] R. J. DHOLAKIA, F. DRAKOPOULOS, C. SADASIVAN, X. JIAO, D. J. FIORELLA, H. H. WOO, B. B. LIEBER, AND N. CHRISOCHOIDES, *High fidelity image-to-mesh conversion for brain aneurysm/stent geometries*, in *IEEE International Symposium on Biomedical Imaging: From Nano to Macro*, Brooklyn, NY, USA, 2015.
- [26] R. J. DHOLAKIA, A. PAGANO, F. DRAKOPOULOS, A. KAPPEL, C. SADASIVAN, X. JIAO, D. J. FIORELLA, N. CHRISOCHOIDES, H. H. WOO, AND B. B. LIEBER, *In vitro and computational fluid dynamics comparison of the flow diversion efficacy of five commercial stents*, in *Summer Biomechanics, Bioengineering, and Biotransport Conference*, Snowbird, Utah, USA, 2015.
- [27] F. DRAKOPOULOS, Y. LIU, K. GARNER, AND N. CHRISOCHOIDES, *Image-to-mesh conversion method for multi-tissue medical image computing simulations*, *Engineering with Computers*, (2024).
- [28] F. DRAKOPOULOS, C. TSOLAKIS, AND N. CHRISOCHOIDES, *Fine-grained speculative topological transformation scheme for local reconnection methods*, *AIAA Journal*, 57 (2019), pp. 4007–4018.
- [29] A. FEDOROV AND N. CHRISOCHOIDES, *Tetrahedral mesh generation for non-rigid registration of brain mri: Analysis of the requirements and evaluation of solutions*, in *Proceedings of the 17th International Meshing Roundtable*, R. V. Garimella, ed., Berlin, Heidelberg, 2008, Springer Berlin Heidelberg, pp. 55–72.
- [30] P. FOTEINOS AND N. CHRISOCHOIDES, *4d space-time Delaunay meshing for medical images*, in *Proceedings of the 22nd International Meshing Roundtable*, J. Sarate and M. Staten, eds., Cham, 2014, Springer International Publishing, pp. 223–240.

- [31] P. A. FOTEINOS AND N. P. CHRISOCHOIDES, *High quality real-time image-to-mesh conversion for finite element simulations*, Journal of Parallel and Distributed Computing, 74 (2014), pp. 2123–2140.
- [32] P. A. FOTEINOS, Y. LIU, A. N. CHERNIKOV, AND N. P. CHRISOCHOIDES, *An evaluation of tetrahedral mesh generation for nonrigid registration of brain mri*, (2011), pp. 131–142.
- [33] L. FREITAG, P. M. KNUPP, T. S. MUNSON, AND S. SHONTZ, *A comparison of optimization software for mesh shape-quality improvement problems*, in 11th International Meshing Roundtable, Ithaca, NY, USA, 2002, pp. 29–40.
- [34] M. FUCHS, M. WAGNER, AND J. KASTNER, *Boundary element method volume conductor models for eeg source reconstruction*, Clinical Neurophysiology, 112 (2001), pp. 1400–1407.
- [35] K. GARNER, C. TSOLAKIS, P. THOMADAKIS, AND N. CHRISOCHOIDES, *Towards distributed semi-speculative adaptive anisotropic parallel mesh generation*, in AIAA Aviation Forum 2024, Las Vegas, NV, USA, 2024. AIAA 2024-4505.
- [36] T. J. GUNDETT, A. L. MARSDEN, W. YANG, AND J. LADISA, JOHN F., *Optimization of Cardiovascular Stent Design Using Computational Fluid Dynamics*, Journal of Biomechanical Engineering, 134 (2012), p. 011002.
- [37] K. HU, Y. J. ZHANG, AND G. XU, *Cvt-based 3d image segmentation and quality improvement of tetrahedral/hexahedral meshes using anisotropic gjauinta-hildebrandt operator*, Computer Methods in Biomechanics and Biomedical Engineering: Imaging & Visualization, 6 (2018), pp. 331–342.
- [38] C.-S. JHUN, R. NEWSWANGER, J. P. CYSYK, S. PONNALURI, B. GOOD, K. B. MANNING, AND G. ROSENBERG, *Dynamics of blood flows in aortic stenosis: Mild, moderate, and severe*, ASAIO Journal, 67 (2021), pp. 666–674.
- [39] B. JOSHI, A. FEDOROV, N. CHRISOCHOIDES, S. K. WARFIELD, AND S. OURSELIN, *A quantitative assessment of approaches to mesh generation for surgical simulation*, Engineering with Computers, 24 (2008), p. 417–430.
- [40] M. KAZAKIDI, F. DRAKOPOULOS, C. SADASIVAN, N. CHRISOCHOIDES, J. EKATERINARIS, AND B. B. LIEBER, *Numerical simulation of cerebral aneurysm by flow diversion*, in European Congress on Computational Methods in Applied Sciences and Engineering, Workshop on Simulation of Cardiovascular Procedures and Devices, Crete, Greece, 2016.
- [41] M. KHAN, V. TORO ARANA, M. NAJAFI, D. MACDONALD, T. NATARAJAN, K. VALEN-SENDSTAD, AND D. STEINMAN, *On the prevalence of flow instabilities from high-fidelity computational fluid dynamics of intracranial bifurcation aneurysms*, Journal of Biomechanics, 127 (2021), p. 110683.
- [42] F. LABELLE AND J. R. SHEWCHUK, *Isosurface stuffing: fast tetrahedral meshes with good dihedral angles*, in ACM Transactions on Graphics (TOG), vol. 26, ACM, 2007, p. 57.
- [43] W. LEI, C. SADASIVAN, X. GU, AND S. CHEN, *Cfd-driven topology optimization for personalized intracranial aneurysm implant design*, in International Design Engineering Technical Conferences & Computers & Information in Engineering Conference, Washington DC, USA, August 2024. IDETC/CIE2024-143347.
- [44] X. LIANG AND Y. ZHANG, *An octree-based dual contouring method for triangular and tetrahedral mesh generation with guaranteed angle range*, Engineering with Computers, 30 (2014), pp. 211–222.
- [45] T. LIAO, Y. ZHANG, P. M. KEKENES-HUSKEY, Y. CHENG, A. MICHAILOVA, A. D. MCCULLOCH, M. HOLST, AND J. A. MCCAMMON, *Multi-core CPU or GPU-accelerated multiscale modeling for biomolecular complexes*, Computational and Mathematical Biophysics, 1 (2013), pp. 164–179.
- [46] Y. LIU, P. FOTEINOS, A. CHERNIKOV, AND N. CHRISOCHOIDES, *Mesh deformation-based multi-tissue mesh generation for brain images*, Engineering with Computers, 28 (2012), pp. 305–318.
- [47] D. L. MARCUM, *Anisotropic solution adaptive unstructured grid generation using aftr*, Tech. Rep. 20070018160, NASA Langley Research Center, Hampton, VA, USA, 2007.
- [48] D. L. MARCUM AND F. ALAUZET, *Unstructured mesh generation using advancing layers and metric-based transition for viscous flowfields*, in 21st AIAA Computational Fluid Dynamics Conference, San Diego, CA, USA, 2013, AIAA. AIAA 2013-2710.
- [49] D. L. MARCUM AND N. P. WEATHERILL, *Unstructured grid generation using iterative point insertion and local reconnection*, AIAA Journal, 33 (1995). <https://doi.org/10.2514/3.12701>.
- [50] N. MOLINO, R. BRIDSON, J. TERAN, AND R. FEDKIW, *A crystalline, red green strategy for meshing highly deformable objects with tetrahedra*, in 12th International Meshing Roundtable, Santa Fe, NM, USA, 2003, pp. 103–114.
- [51] D. MUKHERJEE, N. D. JANI, J. NARVID, AND S. C. SHADDEN, *The role of circle of willis anatomy variations in cardio-embolic stroke: A patient-specific simulation based study*, Annals of Biomedical Engineering, 46 (2018), pp. 1128–1145.
- [52] Y. MURAYAMA, S. FUJIMURA, T. SUZUKI, AND H. TAKAO, *Computational fluid dynamics as a risk assessment tool for aneurysm rupture*, Neurosurgical Focus, 47 (2019), p. E12.
- [53] V. M. PEREIRA, P. LYLYK, N. CANCELLIERE, P. N. LYLYK, I. LYLYK, V. ANAGNOSTAKOU, C. BLEISE, H. NISHI, M. EPSHTEIN, R. M. KING, M. S. SHAZEEB, A. S. PURI, C. W. LIANG, R. A. HANEL, J. SPEARS, T. R. MAROTTA, D. K. LOPES, M. J. GOUNIS, AND G. J. UGHI, *Volumetric microscopy of cerebral arteries with a miniaturized optical coherence tomography imaging probe*, Science Translational Medicine, 16 (2024), p. ead14497.



- [54] R. PEWOWARUK, L. LAMERS, AND A. ROLDÁN-ALZATE, *Accelerated estimation of pulmonary artery stenosis pressure gradients with distributed lumped parameter modeling vs. 3d cfd with instantaneous adaptive mesh refinement: Experimental validation in swine*, *Annals of Biomedical Engineering*, 49 (2021), p. 2365–2376.
- [55] R. PEWOWARUK, Y. LI, D. ROWINSKI, AND A. ROLDÁN-ALZATE, *Solution adaptive refinement of cut-cell cartesian meshes can improve fda nozzle computational fluid dynamics efficiency*, *Numerical Methods in Biomedical Engineering*, 37 (2021).
- [56] J.-P. PONS, F. SÉGONNE, J.-D. BOISSONNAT, L. RINEAU, M. YVINEC, AND R. KERIVEN, *High-quality consistent meshing of multi-label datasets*, in *Biennial International Conference on Information Processing in Medical Imaging*, Springer, 2007, pp. 198–210.
- [57] R. RADOVITZKY AND M. ORTIZ, *Tetrahedral mesh generation based on node insertion in crystal lattice arrangements and advancing-front-Delaunay triangulation*, *Computer Methods in Applied Mechanics and Engineering*, 187 (2000), pp. 543–569.
- [58] L. RINEAU AND M. YVINEC, *A generic software design for Delaunay refinement meshing*, *Computational Geometry*, 38 (2007), pp. 100–110.
- [59] L. SHAHID, J. RICE, H. BERHANE, C. RIGSBY, J. ROBINSON, L. GRIFFIN, M. MARKL, AND A. ROLDÁN-ALZATE, *Enhanced 4d flow mri-based cfd with adaptive mesh refinement for flow dynamics assessment in coarctation of the aorta*, *Annals of Biomedical Engineering*, 50 (2022), pp. 1001–1016.
- [60] J. R. SHEWCHUK, *Tetrahedral mesh generation by Delaunay refinement*, in *Proceedings of the Fourteenth Annual Symposium on Computational Geometry, SCG '98*, New York, NY, USA, 1998, ACM, pp. 86–95.
- [61] H. SI, *Adaptive tetrahedral mesh generation by constrained Delaunay refinement*, *International Journal for Numerical Methods in Engineering*, 75 (2008), pp. 856–880.
- [62] D. A. STEINMAN, M. J. GOUNIS, AND M. R. LEVITT, *You're so vein, you probably think this model's about you: opportunities and challenges for computational fluid dynamics in cerebral venous disease*, *Journal of Neurointerventional Surgery*, 15 (2023), pp. 621–622.
- [63] P. THOMADAKIS AND N. CHRISOCHOIDES, *Experience with distributed memory delaunay-based image-to-mesh conversion implementation*, 2023.
- [64] C. TSOLAKIS AND N. CHRISOCHOIDES, *Speculative anisotropic mesh adaptation on shared memory for cfd applications*, *Engineering with Computers*, (2024).
- [65] C. TSOLAKIS, N. CHRISOCHOIDES, M. A. PARK, A. LOSEILLE, AND T. MICHAL, *Parallel anisotropic unstructured grid adaptation*, *AIAA Journal*, 59 (2021), pp. 4764–4776.
- [66] H. ZHANG, Y. JIAO, E. JOHNSON, L. ZHAN, Y. ZHANG, AND K. SHIMADA, *Modelling anisotropic material property of cerebral aneurysms for fluid-structure interaction simulation*, *Computer Methods in Biomechanics and Biomedical Engineering: Imaging & Visualization*, 1 (2013), pp. 164–174.
- [67] Y. ZHANG, *Challenges and advances in image-based geometric modeling and mesh generation*, in *Image-Based Geometric Modeling and Mesh Generation, Lecture Notes in Computational Vision and Biomechanics*, Dordrecht, Netherlands, 2013, Springer Dordrecht, pp. 1–10.
- [68] ———, *Geometric Modeling and Mesh Generation from Scanned Images*, Chapman & Hall, Boca Raton, FL, USA, 2016.
- [69] Y. ZHANG, C. BAJAJ, AND B.-S. SOHN, *3d finite element meshing from imaging data*, *Computer Methods in Applied Mechanics and Engineering*, 194 (2005), pp. 5083–5106.
- [70] Y. ZHANG, T. J. HUGHES, AND C. L. BAJAJ, *An automatic 3d mesh generation method for domains with multiple materials*, *Computer Methods in Applied Mechanics and Engineering*, 199 (2010), pp. 405–415. *Computational Geometry and Analysis*.
- [71] Y. ZHANG AND J. QIAN, *Resolving topology ambiguity for multiple-material domains*, *Computer Methods in Applied Mechanics and Engineering*, 247 (2012), pp. 166–178.